30. Cosmic Rays

Revised October 2021 by J.J. Beatty (Ohio State U.), J. Matthews (Louisiana State U.) and S.P. Wakely (Chicago U.; Chicago U., Kavli Inst.).

Cosmic rays are a population of energetic elementary particles and nuclei with a steeply falling, nearly power-law spectrum extending from a few MeV to tens of J per particle. Primary cosmic rays can be measured directly by experiments in space or on balloons at energies where there is sufficient flux (§30.1). Atmospheric interactions of primary cosmic rays produce fluxes of secondary elementary particles which can be detected in the atmosphere (§30.2), at the Earth's surface (§30.3), and underground (§30.4). At high energies, air showers of particles generated by a single primary can be detected (§30.5). These showers can be reconstructed to determine the energy, direction, and composition of the incident particle. Gamma-ray photons are observed both as diffuse fluxes and as steady-state and transient emission from sources (§30.6). Energetic neutrinos are closely linked to high energy protons and nuclei, both through production at astrophysical sites of particle acceleration and by production during propagation of extremely high energy particles (§30.7).

30.1 Primary Spectra from Direct Measurements

The cosmic radiation incident at the top of the terrestrial atmosphere includes all stable charged particles and nuclei with lifetimes of order 10^6 years or longer. When discussing the astrophysical origin of cosmic rays, "primary" cosmic rays are those particles accelerated at astrophysical sources and "secondaries" are those particles produced in interaction of the primaries with interstellar gas[1]. Thus electrons, protons and helium, as well as carbon, oxygen, iron, and other nuclei synthesized in stars, are primaries. Nuclei such as lithium, beryllium, and boron (which are not abundant end-products of stellar nucleosynthesis) are secondaries. Antiprotons and positrons are also in large part secondary. Whether a small fraction of these particles may be primary is a question of current interest.

There are four different ways to describe the spectra of the components of the cosmic radiation: (1) By particles per unit rigidity. Propagation (and probably also acceleration) through cosmic magnetic fields depends on the gyroradius or *magnetic rigidity, R*, which is the gyroradius multiplied by the magnetic field strength:

$$R = \frac{p\,c}{Z\,e} = r_{_L} B \tag{30.1}$$

(2) By particles per energy-per-nucleon. Fragmentation of nuclei propagating through the interstellar gas depends on the energy per nucleon, since that quantity is approximately conserved when a nucleus breaks up on interaction with the gas. (3) By nucleons per energy-per-nucleon. Production of secondary cosmic rays in the atmosphere depends on the intensity of nucleons per energy-per-nucleon, approximately independently of whether the incident nucleons are free protons or bound in nuclei. (4) By particles per energy-per-nucleus. Air shower experiments that use the atmosphere as a calorimeter generally measure a quantity that is related to total energy per particle.

The units of differential intensity I are $[\mathrm{m}^{-2}\,\mathrm{s}^{-1}\mathrm{sr}^{-1}\mathcal{E}^{-1}]$, where $\mathcal{E}$ represents the units of one of the four variables listed above.

Apart from particles associated with solar flares[2], the cosmic radiation comes from outside the solar system. The incoming charged particles are "modulated" by the solar wind, the expanding magnetized plasma generated by the Sun, which decelerates and partially excludes the lower energy

[1] 'Primary' and 'secondary' are used in a different but analogous sense when discussing cosmic ray interactions in the atmosphere.

[2] Energetic particles accelerated by the Sun and at other sites within the heliosphere and at its boundary are outside the scope of this review.

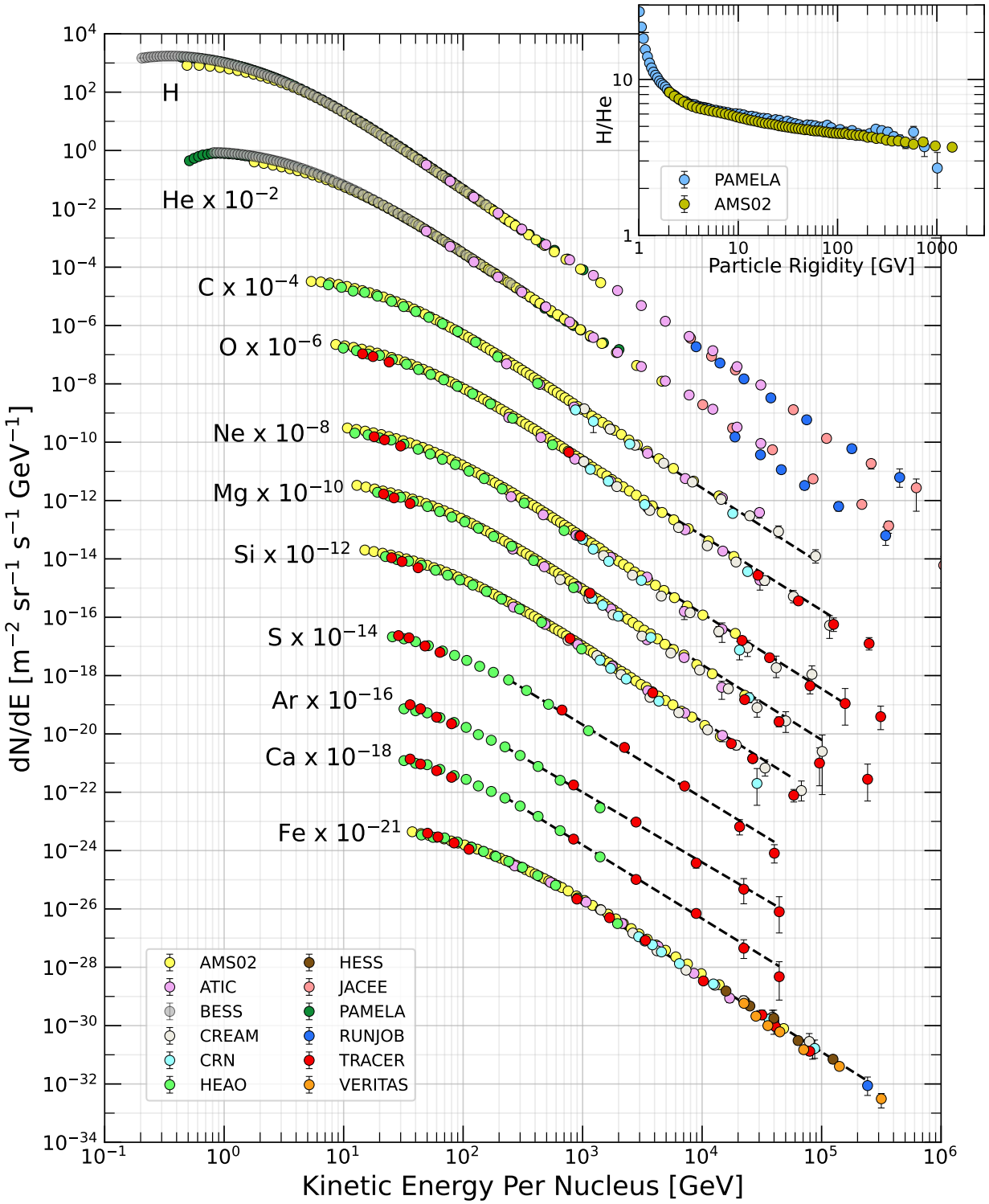

Figure 30.1: Fluxes of nuclei of the primary cosmic radiation in particles per energy-per-nucleus are plotted vs energy-per-nucleus using data from Refs. [1–15] The inset shows the H/He ratio as a function of rigidity [1, 3].

Galactic cosmic rays from the inner solar system. There is a significant anti-correlation between solar activity (which has an alternating eleven-year cycle) and the intensity of the cosmic rays with rigidities below about 10 GV. In addition, the lower-energy cosmic rays are affected by the geomagnetic field, which they must penetrate to reach the top of the atmosphere. Thus the intensity of any component of the cosmic radiation in the GeV range depends both on the location and time.

The intensity of primary nucleons in the energy range from several GeV to somewhat beyond 100 TeV is given approximately by

$$I_N(E) \;\approx\; 1.8 \times 10^4 \; (E/1 \text{ GeV})^{-\alpha} \; \frac{\text{nucleons}}{\text{m}^2 \text{ s sr GeV}}, \tag{30.2}$$

where E is the energy-per-nucleon (including rest mass energy), α ($\equiv \gamma + 1$) ≈ 2.7 is the differential spectral index of the cosmic-ray flux, and γ is the integral spectral index. About 74% of the primary nucleons are free protons and about 70% of the rest are nucleons bound in helium nuclei. The fractions of the primary nuclei are nearly constant over this energy range. Fractions of both primary and secondary incident nuclei are listed in Table 30.1. Figure 30.1 shows the major nuclear components for kinetic energies greater than 0.22 GeV/nucleus. Figure 30.2 shows the relative abundances of low-energy ($\tilde{0}$.2 GeV/nucleon) cosmic rays compared to the present-day solar system. Secondary cosmic rays contribute to increased abundances of rare elements and a reduced even-odd effect. A useful compendium of experimental data for cosmic-ray nuclei and electrons is described in [16].

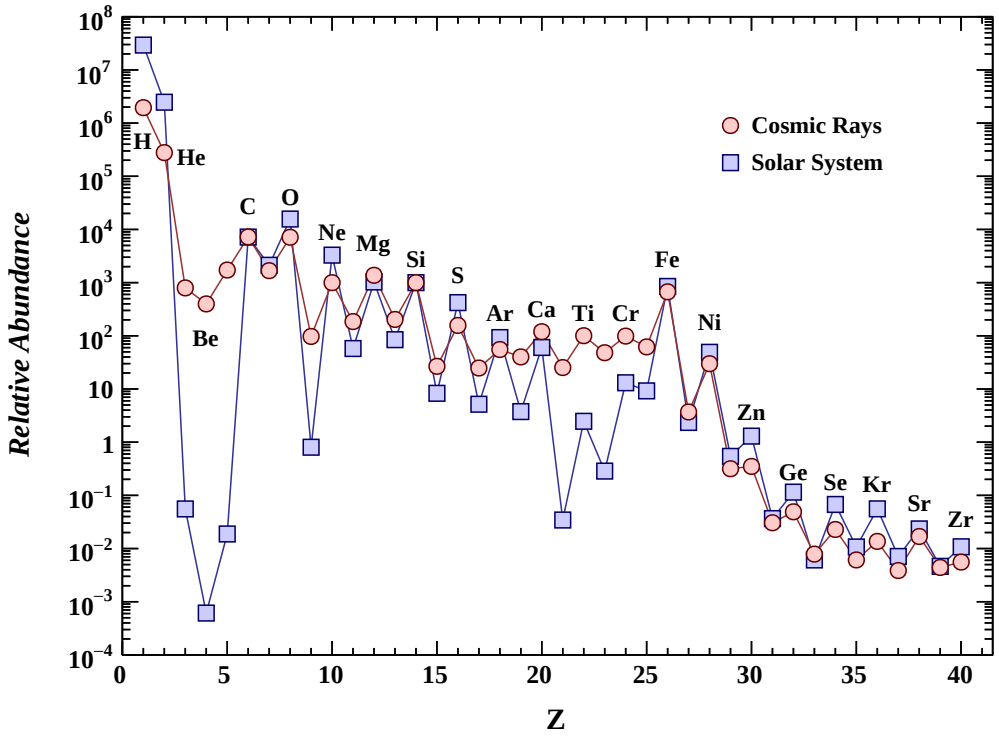

Figure 30.2: Cosmic ray elemental abundances compared to abundances in present-day solar system material. Abundances are normalised to Si=10^3. Cosmic ray abundances are from AMS-02 (H,He) [3,17], ACE/CRIS (Li-Ni) [18,19], and TIGER/SuperTIGER (Cu-Zr) [20,21]. Solar system abundances are from Table 6 of Ref. [22].

Table 30.1: Relative abundances F of cosmic-ray nuclei at 10.6 GeV/nucleon normalized to oxygen ($\equiv 1$) [9]. The oxygen flux at kinetic energy of 10.6 GeV/nucleon is 3.29×10^{-2} (m^2 s sr GeV/nucleon)$^{-1}$. Abundances of hydrogen and helium are from Refs. [2–4]. Note that one can not use these values to extend the cosmic-ray flux to high energy because the power law indices for each element may differ slightly.

Z	Element	F	Z	Element	F
1	H	550	13–14	Al-Si	0.19
2	He	34	15–16	P-S	0.03
3–5	Li-B	0.40	17–18	Cl-Ar	0.01
6–8	C-O	2.20	19–20	K-Ca	0.02
9–10	F-Ne	0.30	21–25	Sc-Mn	0.05
11–12	Na-Mg	0.22	26–28	Fe-Ni	0.12

The composition and energy spectra of nuclei are typically interpreted in the context of propagation models, in which the sources of the primary cosmic radiation are located within the Galaxy [23]. The ratio of secondary to primary nuclei is observed to decrease with increasing energy, a fact often interpreted to mean that the lifetime of cosmic rays in the Galaxy decreases with energy. Measurements of radioactive "clock" isotopes in the low energy cosmic radiation are consistent with a lifetime in the Galaxy of about 15 Myr [24].

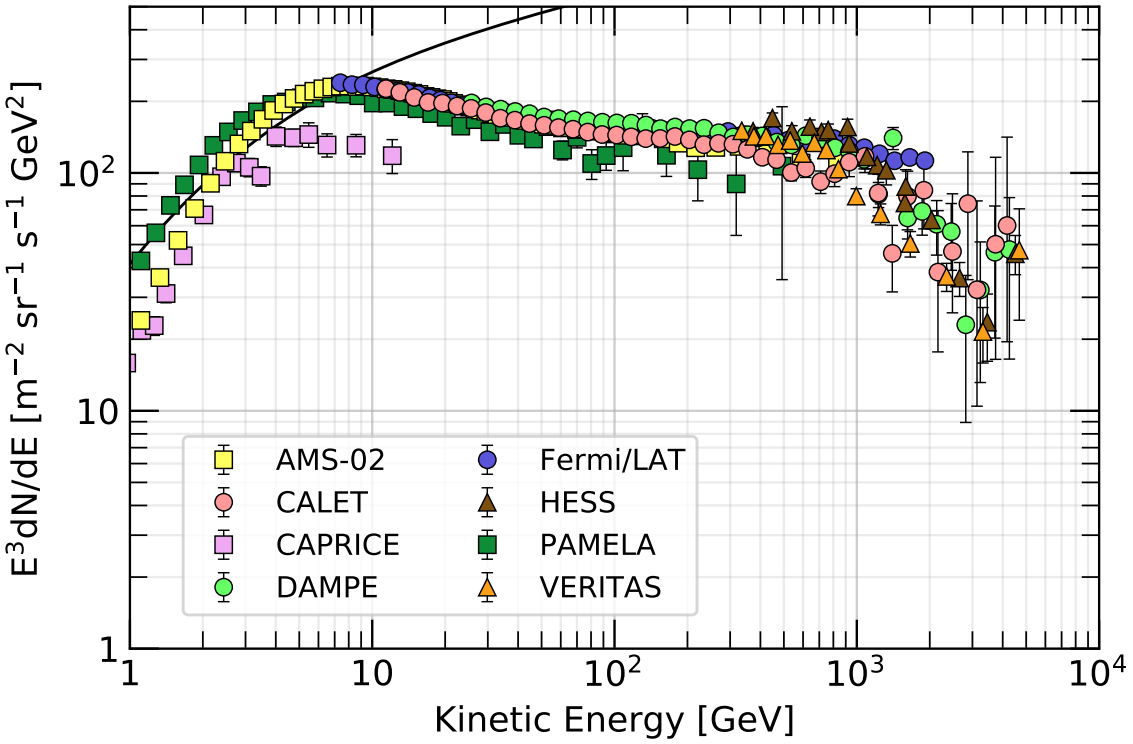

Figure 30.3: Differential spectrum of electrons plus positrons (except PAMELA data, which are electrons only) multiplied by E^3 [25–33] The line shows the proton spectrum [34] multiplied by 0.01.

Cosmic rays are nearly isotropic at most energies due to diffusive propagation in the Galactic magnetic field. Several collaboratiions [35–39] have observed anisotropy on various angular scales at the level of about 10^{-3} for cosmic rays with energy of a few TeV, possibly due the direction of local Galactic magnetic fields, motion of the solar system in the Galaxy, and to the distribution of sources [40].

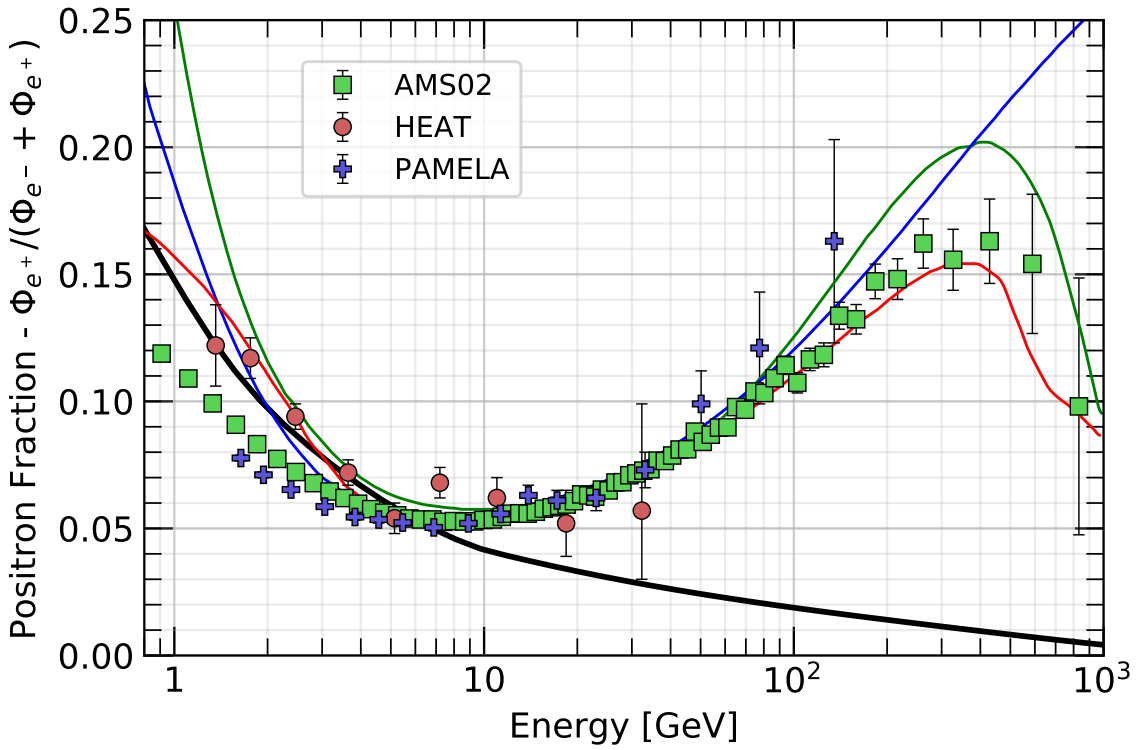

Figure 30.4: The positron fraction (ratio of the flux of e^+ to the total flux of e^+ and e^-) [27,41–43]. The heavy black line is a model of pure secondary production [44] and the three thin lines show three representative attempts to model the positron excess with different phenomena: green: dark matter decay [45]; blue: propagation physics [46]; red: production in pulsars [47]. The ratio below 10 GeV is dependent on the intensity and polarity of the solar magnetic field.

The spectrum of electrons and positrons incident at the top of the atmosphere is generally expected to steepen by one power of E above an energy of 5 GeV because of radiative energy loss effects in the Galaxy. Most modern measurements of the combined electron+positron spectrum at high energy, which includes data from spectrometers, calorimeters, and ground-based air Cherenkov telescopes, reveal a relatively smooth spectrum to approximately 1 TeV, where evidence of a cutoff has been reported [29, 31, 33].

The PAMELA [41, 42] and AMS-02 [48, 49] satellite experiments measured the positron to electron ratio to increase above 10 GeV instead of the expected decrease [44] at higher energy, confirming earlier hints seen by the HEAT balloon-borne experiment [43]. The structure in the electron spectrum, as well as the increase in the positron fraction, may be related to contributions from individual nearby sources (supernova remnants or pulsars) emerging above a background suppressed at high energy by synchrotron losses [50]. Other explanations have invoked propagation effects [46] or dark matter decay/annihilation processes (see, e.g., [45]). The significant disagreement in the ratio below ∼10 GeV is attributable to differences in charge-sign dependent solar modulation effects present near Earth at the times of measurement.

The ratio of antiprotons to protons is $\sim 2 \times 10^{-4}$ [51] at around 10–20 GeV, and there is clear evidence [52] for the kinematic suppression at lower energy that is the signature of secondary antiprotons. The $\overline{p}/p$ ratio also shows a strong dependence on the phase and polarity of the solar cycle [53] in the opposite sense to that of the positron fraction. There is at this time no evidence for a significant primary component of antiprotons. No antihelium or antideuteron has been found in the cosmic radiation. The best measured upper limit on the ratio antihelium/helium is currently approximately 1×10^{-7} [54] The upper limit on the flux of antideuterons around 1 GeV/nucleon is approximately $2 \times 10^{-4}\,(\mathrm{m^2\ s\ sr\ GeV/nucleon})^{-1}$ [55].

A useful method for calculating the effect of solar modulation including time, charge-sign, and rigidity-dependent effects is given in Ref. [56].

30.2 Cosmic Rays in the Atmosphere

Figure 30.5 shows the vertical fluxes of the major cosmic-ray components in the atmosphere in the energy region where the particles are most numerous (except for electrons, which are most numerous near their critical energy, which is about 81 MeV in air). Except for protons and electrons near the top of the atmosphere, all particles are produced in interactions of the primary[3] cosmic rays in the air. Muons and neutrinos are products of the decay chain of charged mesons, while electrons and photons originate in decays of neutral mesons.

Most measurements are made at ground level or near the top of the atmosphere, but there are also measurements of muons and electrons from airplanes and balloons. Fig. 30.5 shows measurements of negative muons [57–62]. Since $\mu^+(\mu^-)$ are produced in association with $\nu_\mu(\overline{\nu}_\mu)$, the measurement of muons near the maximum of the intensity curve for the parent pions serves to calibrate the atmospheric $\nu_\mu(\overline{\nu}_\mu)$ beam [63]. Because muons typically lose almost 2 GeV in passing through the atmosphere, the comparison near the production altitude is important for the sub-GeV range of $\nu_\mu(\overline{\nu}_\mu)$ energies.

The flux of cosmic rays through the atmosphere is described by a set of coupled cascade equations with boundary conditions at the top of the atmosphere to match the primary spectrum. Numerical or Monte Carlo calculations are needed to account accurately for decay and energy-loss processes, and for the energy-dependences of the cross sections and of the primary spectral index γ. Approximate analytic solutions are, however, useful in limited regions of energy [64, 65]. For example, the vertical intensity of charged pions with energy $E_\pi \ll \epsilon_\pi = 115$ GeV is

$$I_\pi(E_\pi, X) \;\approx\; \frac{Z_{N\pi}}{\lambda_N}\, I_N(E_\pi, 0)\, e^{-X/\Lambda\, \frac{X\, E_\pi}{\epsilon_\pi}} \tag{30.3}$$

where Λ is the characteristic length for exponential attenuation of the parent nucleon flux in the atmosphere. This expression has a maximum at $X = \Lambda \approx 121 \pm 4$ g cm^{-2} [66], which corresponds to an altitude of 15 kilometers. The quantity $Z_{N\pi}$ is the spectrum-weighted moment that characterizes the inclusive distribution of charged pions in interactions of a spectrum of nucleons with nuclei of the atmosphere. The intensity of low-energy pions is much less than that of nucleons because $Z_{N\pi} \approx 0.079$ is small and because most pions with energy much less than the critical energy ϵ_π decay rather than interact.

[3] When discussing cosmic rays in the atmosphere, 'primary' is used to denote the original particle and 'secondary' to denote the particles produced in interactions.

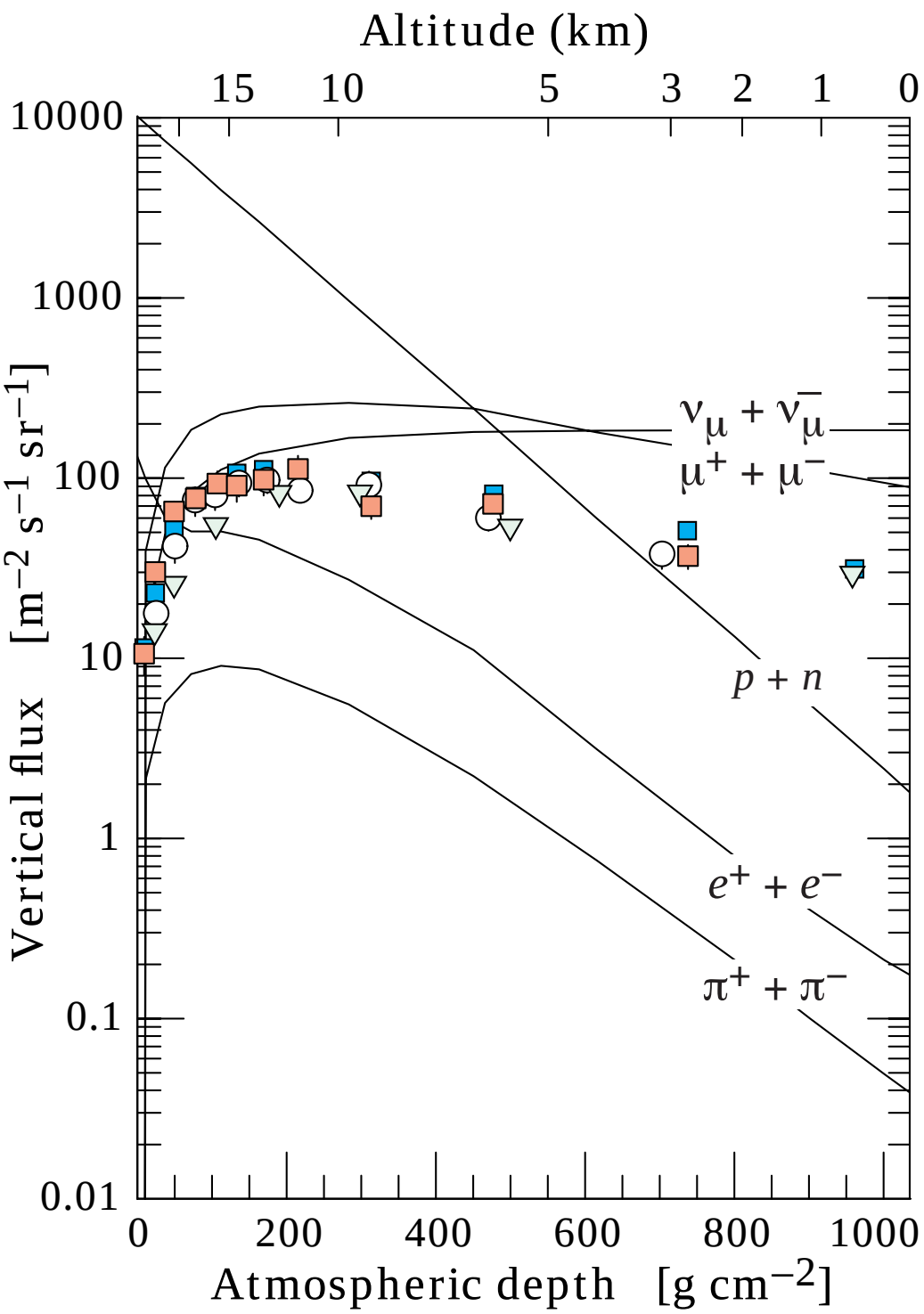

Figure 30.5: Vertical fluxes of cosmic rays in the atmosphere with $E > 1$ GeV estimated from the nucleon flux of Eq. (30.2). The experimental points show measurements of negative muons with $E_\mu > 1$ GeV [57–62].

30.3 Cosmic rays at the surface

30.3.1 *Muons*

Muons are the most numerous charged particles at sea level (see Fig. 30.5). Most muons are produced high in the atmosphere (typically 15 km) and lose about 2 GeV to ionization before reaching the ground. Their energy and angular distribution reflect a convolution of the production spectrum, energy loss in the atmosphere, and decay. For example, 2.4 GeV muons have a decay length of 15 km, which is reduced to 8.7 km by energy loss. The mean energy of muons at the ground is ≈ 4 GeV. The energy spectrum is almost flat below 1 GeV, steepens gradually to reflect the primary spectrum in the 10–100 GeV range, and steepens further at higher energies because pions with $E_\pi > \epsilon_\pi$ tend to interact in the atmosphere before they decay. Asymptotically ($E_\mu \gg 1$ TeV), the energy spectrum of atmospheric muons is one power steeper than the primary spectrum. The integral intensity of vertical muons above 1 GeV/c at sea level is ≈ 70 m^{-2}s^{-1}sr^{-1} [67, 68], with recent measurements [62, 69, 70] favoring a lower normalization by 10-15%. Experimentalists are familiar with this number in the form $I \approx 1$ cm^{-2} min^{-1} for horizontal detectors. The overall angular distribution of muons at the ground as a function of zenith angle θ is $\propto \cos^2\theta$, which is characteristic of muons with $E_\mu \sim 3$ GeV. At lower energy the angular distribution becomes increasingly steep, while at higher energy it flattens, approaching a $\sec\theta$ distribution for $E_\mu \gg \epsilon_\pi$ and $\theta < 70°$.

Figure 30.6 shows the muon energy spectrum at sea level for two angles. At large angles low energy muons decay before reaching the surface and high energy pions decay before they interact, thus the average muon energy increases. An approximate extrapolation formula valid when muon decay is negligible ($E_\mu > 100/\cos\theta$ GeV) and the curvature of the Earth can be neglected ($\theta < 70°$)

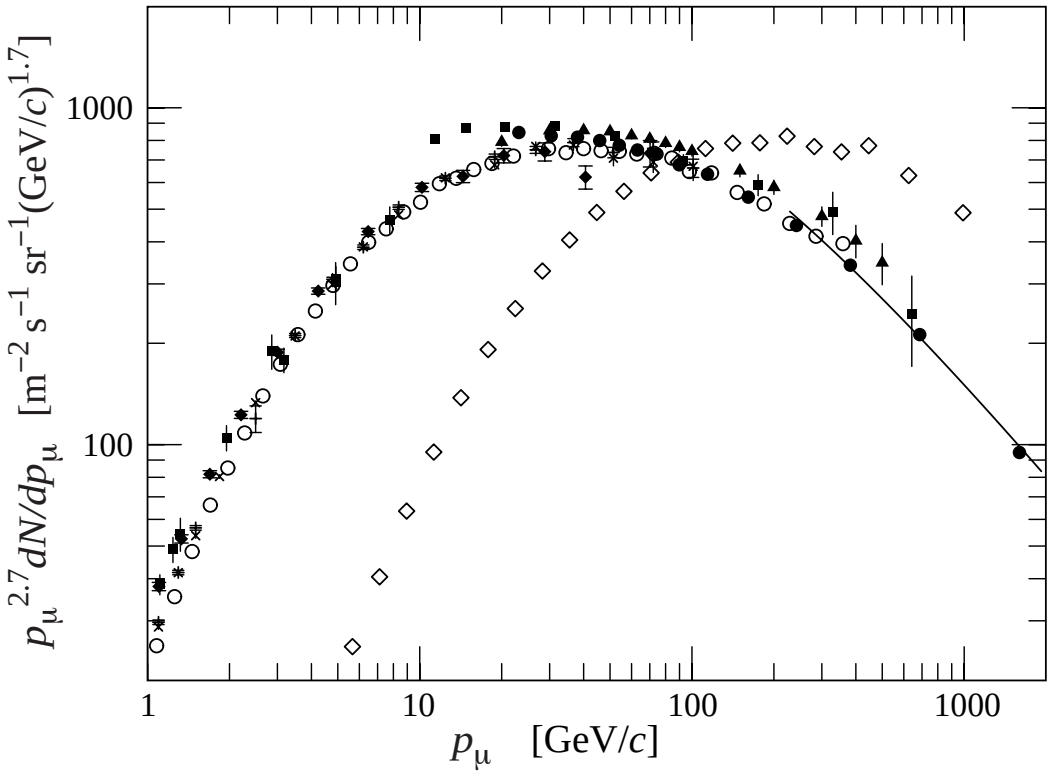

Figure 30.6: Spectrum of muons at $\theta = 0°$ (♦ [67], ■ [71], ▼ [72], ▲ [73], ×, + [69], ○ [62], and • [70] and $\theta = 75°$ ◇ [74]). The line plots the result from Eq. (30.4) for vertical showers.

is

$$\frac{dN_\mu}{dE_\mu d\Omega} \approx \frac{0.14\, E_\mu^{-2.7}}{\mathrm{cm^2\ s\ sr\ GeV}} \times \left\{ \frac{1}{1+\frac{1.1 E_\mu \cos\theta}{115\,\mathrm{GeV}}} + \frac{0.054}{1+\frac{1.1 E_\mu \cos\theta}{850\,\mathrm{GeV}}} \right\} \tag{30.4}$$

where the two terms give the contribution of pions and charged kaons. Eq. (30.4) neglects a small contribution from charm and heavier flavors which is negligible except at very high energy [75].

The muon charge ratio reflects the excess of π^+ over π^- and K^+ over K^- in the forward fragmentation region of proton initiated interactions together with the fact that there are more free and bound protons than free and bound neutrons in the primary spectrum. The increase with energy of μ^+/μ^- shown in Fig. 30.7 reflects the increasing importance of kaons in the TeV range [76] and indicates a significant contribution of associated production by cosmic-ray protons ($p \to \Lambda + K^+$). The same process is even more important for atmospheric neutrinos at high energy.

30.3.2 *Electromagnetic component*

At the ground, this component consists of electrons, positrons, and photons primarily from cascades initiated by decay of neutral and charged mesons. Muon decay is the dominant source of low-energy electrons at sea level. Decay of neutral pions is more important at high altitude or when the energy threshold is high. Knock-on electrons also make a small contribution at low energy [77]. The integral vertical intensity of electrons plus positrons is very approximately 30, 6, and 0.2 $\mathrm{m^{-2}s^{-1}sr^{-1}}$ above 10, 100, and 1000 MeV respectively [68, 78], but the exact numbers depend sensitively on altitude, and the angular dependence is complex because of the different altitude dependence of the different sources of electrons [77, 79]. The ratio of photons to electrons plus positrons is approximately 1.3 above 1 GeV and 1.7 below the critical energy [79].

30.3.3 *Nucleons*

Nucleons above 1 GeV/c at ground level are degraded remnants of the primary cosmic radiation. The intensity is approximately $I_N(E,0) \times \exp(-X/\cos\theta\Lambda)$ for $\theta < 70°$. At sea level, about 1/3 of the nucleons in the vertical direction are neutrons (up from $\approx 10\%$ at the top of the atmosphere as the n/p ratio approaches equilibrium). The integral intensity of vertical protons above 1 GeV/c at sea level is ≈ 0.9 $\mathrm{m^{-2}s^{-1}sr^{-1}}$ [68, 80].

30.4 Cosmic Rays Underground

Only muons and neutrinos penetrate to significant depths underground. The muons produce tertiary fluxes of photons, electrons, and hadrons.

30.4.1 *Muons*

As discussed in Section 34.6 of this *Review*, muons lose energy by ionization and by radiative processes: bremsstrahlung, direct production of e^+e^- pairs, and photonuclear interactions. The

Table 30.2: Average muon range R and energy loss parameters calculated for standard rock. Range is given in km-water-equivalent, or 10^5 g cm^{-2}.

E_μ	R	a	b_{brems}	b_{pair}	b_{nucl}	$\sum b_i$	$\sum b_{\mathrm{ice}}$
GeV	km.w.e.	$\frac{\mathrm{MeV\ cm^2}}{\mathrm{g}}$			10^{-6} g^{-1} cm^2		
10	0.05	2.17	0.70	0.70	0.50	1.90	1.66
10^2	0.41	2.44	1.10	1.53	0.41	3.04	2.51
10^3	2.45	2.68	1.44	2.07	0.41	3.92	3.17
10^4	6.09	2.93	1.62	2.27	0.46	4.35	3.78

total muon energy loss may be expressed as a function of the amount of matter traversed as

$$-\frac{dE_\mu}{dX} = a + b\,E_\mu \tag{30.5}$$

where a is the ionization loss and b is the fractional energy loss by the three radiation processes. Both are slowly varying functions of energy. The quantity $\epsilon \equiv a/b$ (≈ 500 GeV in standard rock) defines a critical energy below which continuous ionization loss is more important than radiative losses. Table 30.2 shows a and b values for standard rock, and b for ice, as a function of muon energy. The second column of Table 30.2 shows the muon range in standard rock ($A = 22$, $Z = 11$, $\rho = 2.65$ g cm^{-3}). These parameters are quite sensitive to the chemical composition of the rock, which must be evaluated for each location.

The intensity of muons underground can be estimated from the muon intensity in the atmosphere and their rate of energy loss. To the extent that the mild energy dependence of a and b can be neglected, Eq. (30.5) can be integrated to provide the following relation between the energy $E_{\mu,0}$ of a muon at production in the atmosphere and its average energy E_μ after traversing a thickness X of rock (or ice or water):

$$E_{\mu,0} = (E_\mu + \epsilon)e^{bX} - \epsilon\ . \tag{30.6}$$

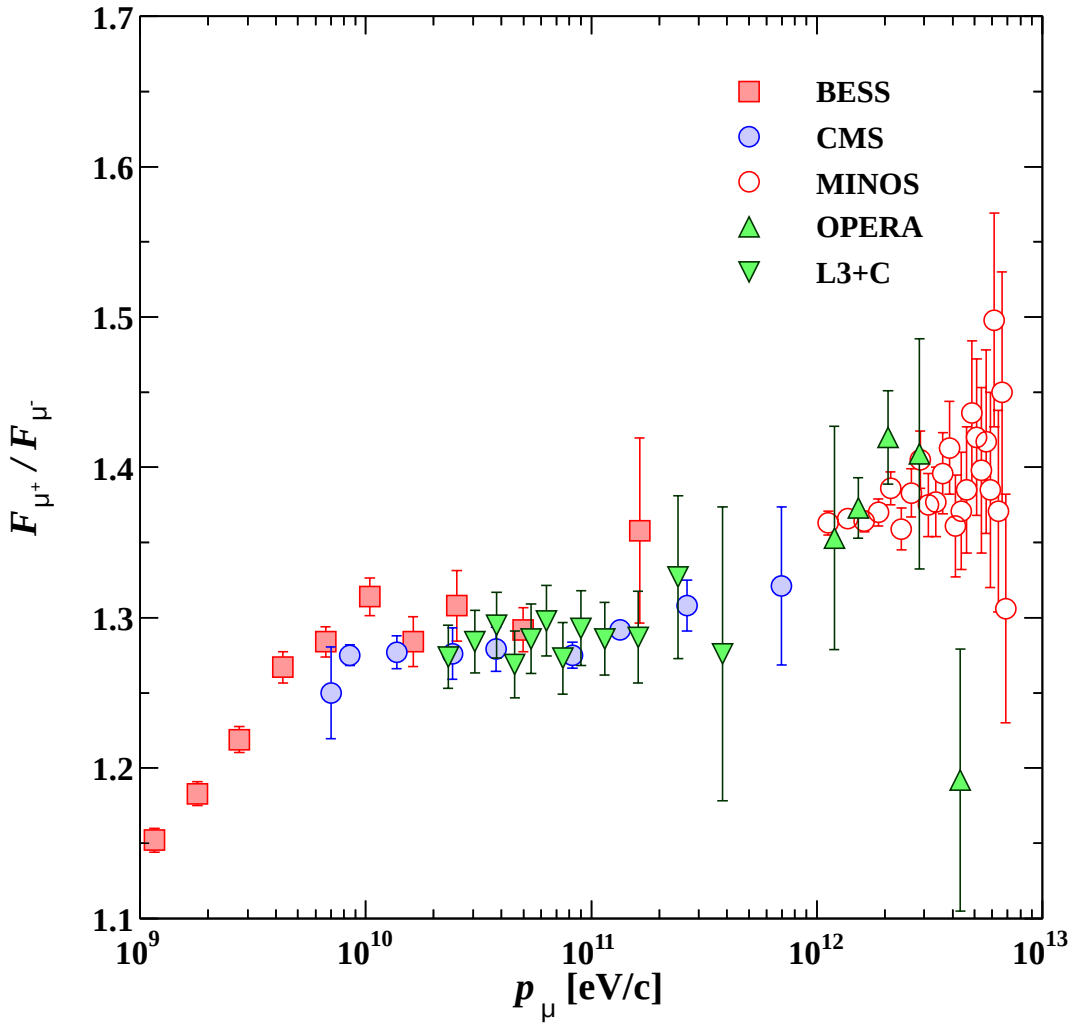

Figure 30.7: Muon charge ratio as a function of the muon momentum from Refs. [62,70,76,81,82].

Table 30.3: Measured fluxes (10^{-9} m^{-2} s^{-1} sr^{-1}) of neutrino-induced muons as a function of the effective minimum muon energy E_μ.

$E_\mu >$	1 GeV	1 GeV	1 GeV	2 GeV	3 GeV	3 GeV
Ref.	CWI [95]	Baksan [96]	MACRO [97,98]	IMB [99,100]	Kam [101]	SuperK [102]
F_μ	2.17±0.21	2.77±0.17	2.29 ± 0.15	2.26±0.11	1.94±0.12	1.74±0.07

Especially at high energy, however, fluctuations are important and an accurate calculation requires a simulation that accounts for stochastic energy-loss processes [83].

There are two depth regimes for which Eq. (30.6) can be simplified. For $X \ll b^{-1} \approx 2.5$ km water equivalent, $E_{\mu,0} \approx E_\mu(X) + aX$, while for $X \gg b^{-1}$ $E_{\mu,0} \approx (\epsilon + E_\mu(X)) \exp(bX)$. Thus at shallow depths the differential muon energy spectrum is approximately constant for $E_\mu < aX$ and steepens to reflect the surface muon spectrum for $E_\mu > aX$, whereas for $X > 2.5$ km-water-equivalent (km.w.e.)] the differential spectrum underground is again constant for small muon energies but steepens to reflect the surface muon spectrum for $E_\mu > \epsilon \approx 0.5$ TeV. In the deep regime the shape is independent of depth although the intensity decreases exponentially with depth. In general the muon spectrum at slant depth X is

$$\frac{dN_\mu(X)}{dE_\mu} = \frac{dN_\mu}{dE_{\mu,0}} \frac{dE_{\mu,0}}{dE_\mu} = \frac{dN_\mu}{dE_{\mu,0}} e^{bX} \tag{30.7}$$

where $E_{\mu,0}$ is the solution of Eq. (30.6) in the approximation neglecting fluctuations.

Fig. 30.8 shows the vertical muon intensity versus depth. In constructing this "depth-intensity curve," each group has taken account of the angular distribution of the muons in the atmosphere, the map of the overburden at each detector, and the properties of the local medium in connecting measurements at various slant depths and zenith angles to the vertical intensity. Use of data from a range of angles allows a fixed detector to cover a wide range of depths. The flat portion of the curve is due to muons produced locally by charged-current interactions of ν_μ. The inset shows the vertical intensity curve for water and ice [90–93]. It is not as steep as the one for rock because of the lower muon energy loss in water.

30.4.2 *Atmospheric Neutrinos*

Because neutrinos have small interaction cross sections, measurements of atmospheric neutrinos require a deep detector to avoid backgrounds. There are two types of measurements: contained (or semi-contained) events, in which the vertex is determined to originate inside the detector, and neutrino-induced muons. The latter are muons that enter the detector from zenith angles so large (*e.g.*, nearly horizontal or upward) that they cannot be muons produced in the atmosphere. In neither case is the neutrino flux measured directly. What is measured is a convolution of the neutrino flux and cross section with the properties of the detector (which includes the surrounding medium in the case of entering muons). This section focuses on neutrinos below about 1 TeV. For discussion of atmospheric neutrinos in the TeV–PeV region including a prompt component produced by charmed meson decays, see Ref. [64].

Contained and semi-contained events reflect neutrinos in the sub-GeV to multi-GeV region where the product of increasing cross section and decreasing flux is maximum. In the GeV region the neutrino flux and its angular distribution depend on the geomagnetic location of the detector and, to a lesser extent, on the phase of the solar cycle. Naively, we expect $\nu_\mu/\nu_e = 2$ from counting neutrinos of the two flavors coming from the chain of pion and muon decays. Contrary to expectation, however, the numbers of the two classes of events are similar rather than different by

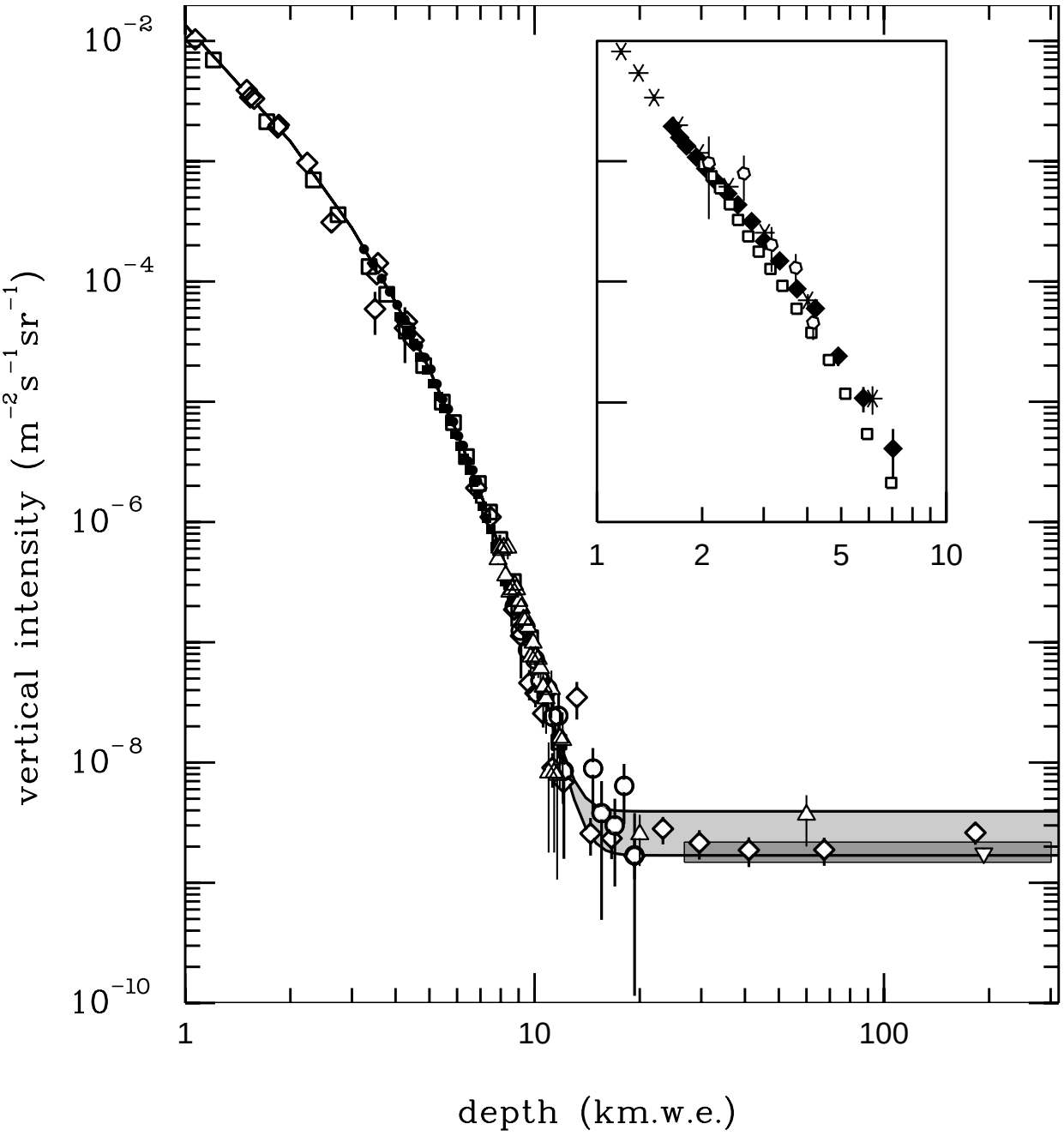

Figure 30.8: Vertical muon intensity vs depth (1 km.w.e. = 10^5 g cm^{-2} of standard rock). The experimental data are from: ♢: the compilations of Crouch [84], □: Baksan [85], ○: LVD [86], ●: MACRO [87], ■: Frejus [88], and △: SNO [89]. The shaded area at large depths represents neutrino-induced muons of energy above 2 GeV. The upper line is for horizontal neutrino-induced muons, the lower one for vertically upward muons. Darker shading shows the muon flux measured by the SuperKamiokande experiment. The inset shows the vertical intensity curve for water and ice published in Refs. [90–93]. Additional data extending to slant depths of 13 km are available in [94].

a factor of two. This is now understood to be a consequence of neutrino flavor oscillations [103]. (See the article on neutrino properties in this *Review*.)

Two well-understood properties of atmospheric cosmic rays provide a standard for comparison of the measurements of atmospheric neutrinos to expectation. These are the "$\sec\theta$ effect" and the "east-west effect" due to the Earth's magnetic field [104]. The former refers originally to the enhancement of the flux of > 10 GeV muons (and neutrinos) at large zenith angles because the parent pions propagate more in the low density upper atmosphere where decay is enhanced relative to interaction. For neutrinos from muon decay, the enhancement near the horizontal becomes important for $E_\nu > 1$ GeV and arises mainly from the increased pathlength through the atmosphere for muon decay in flight. Fig. 14.4 from Ref. [105] shows a comparison between measurement and expectation for the zenith angle dependence of multi-GeV electron-like (mostly ν_e) and muon-like (mostly ν_μ) events separately. The ν_e show an enhancement near the horizontal and approximate equality for nearly upward ($\cos\theta \approx -1$) and nearly downward ($\cos\theta \approx 1$) events. There is, however, a very significant deficit of upward ($\cos\theta < 0$) ν_μ events, which have long pathlengths comparable to the radius of the Earth. This feature is the principal signature for atmospheric neutrino oscillations [103].

Muons that enter the detector from outside after production in charged-current interactions of neutrinos naturally reflect a higher energy portion of the neutrino spectrum than contained events because the muon range increases with energy as well as the cross section. The relevant energy range is $\sim 10 < E_\nu < 1000$ GeV, depending somewhat on angle. Neutrinos in this energy range show a $\sec\theta$ effect similar to muons (see Eq. (30.4)). This causes the flux of horizontal neutrino-induced muons to be approximately a factor two higher than the vertically upward flux. The upper and lower edges of the horizontal shaded region in Fig. 30.8 correspond to horizontal and vertical intensities of neutrino-induced muons. Table 30.3 gives the measured fluxes of upward-moving neutrino-induced muons averaged over the lower hemisphere. Generally the definition of minimum muon energy depends on where it passes through the detector. The tabulated effective minimum energy estimates the average over various accepted trajectories.

30.5 Air Showers

So far we have discussed inclusive or uncorrelated fluxes of various components of the cosmic radiation. An air shower is caused by a single cosmic ray with energy high enough for the cascade that it creates in the atmosphere to be detectable at the ground. The shower has a hadronic core, which acts as a collimated source of electromagnetic sub-showers, generated mostly from $\pi^0 \to \gamma\,\gamma$ decays. The resulting electrons and positrons are the most numerous charged particles in the shower, and are accompanied by about ten times as many photons with a mean energy of ~ 10 MeV. The number of muons, produced by decays of charged mesons, is an order of magnitude lower. Air showers spread over a large area on the ground, and arrays of detectors operated for long times are important for studying cosmic rays with primary energy $E_0 > 100$ TeV, where the low flux makes measurements with small detectors in balloons and satellites impractical.

Greisen [120] gives the following approximate analytic expressions for the numbers and lateral distributions of particles in showers at ground level. The total number of muons N_μ with energies above 1 GeV is

$$N_\mu(> 1\text{GeV}) \approx 0.95 \times 10^5 \left(N_e/10^6\right)^{3/4} \ , \tag{30.8}$$

where N_e is the total number of charged particles in the shower (not just $e^\pm$). The number of muons per square meter, ρ_μ, as a function of the lateral distance r (in meters) from the center of the shower is

$$\rho_\mu = \frac{1.25 N_\mu}{2\pi\Gamma(1.25)} \left(\frac{1}{320}\right)^{1.25} r^{-0.75} \left(1 + \frac{r}{320}\right)^{-2.5} \ , \tag{30.9}$$

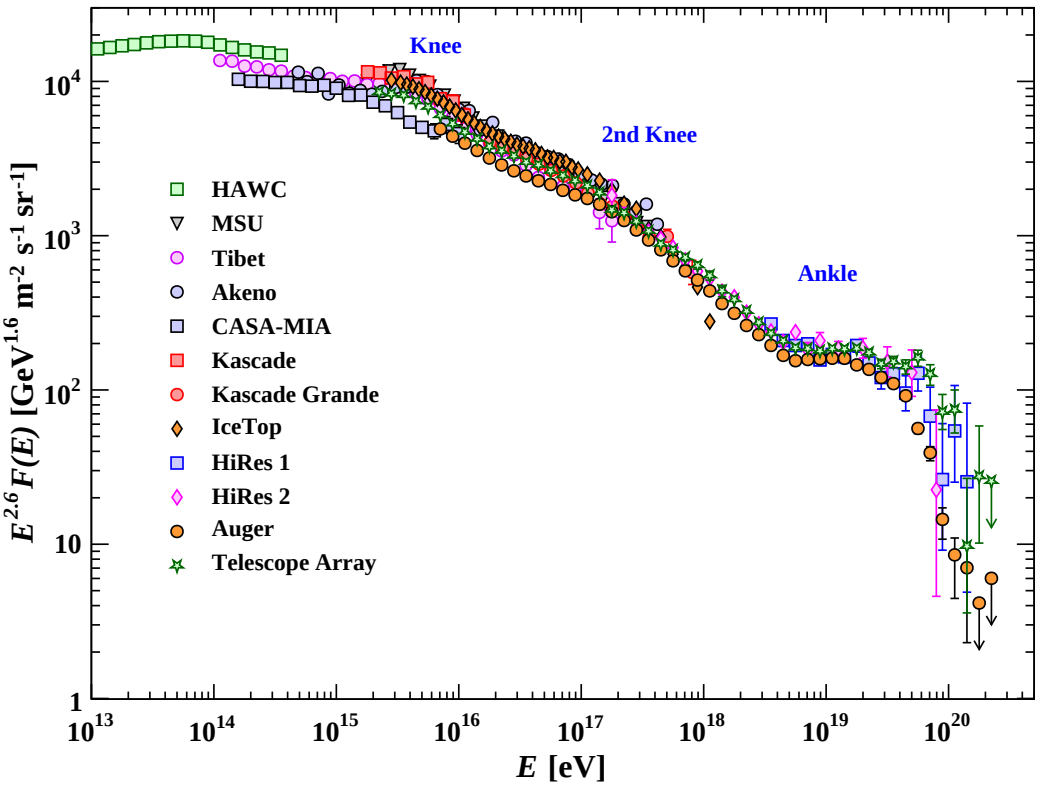

Figure 30.9: The all-particle spectrum as a function of E (energy-per-nucleus) from air shower measurements [106–119]

where Γ is the gamma function. The number density of charged particles is

$$\rho_e = C_1(s,d,C_2)x^{(s-2)}(1+x)^{(s-4.5)}(1+C_2x^d)\ . \tag{30.10}$$

Here s, d, and C_2 are parameters in terms of which the overall normalization constant $C_1(s,d,C_2)$ is given by

$$C_1(s,d,C_2) = \frac{N_e}{2\pi r_1^2}\left[\,B(s,4.5-2s)C_2B(s+d,\,4.5-d-2s)\right]^{-1}\ , \tag{30.11}$$

where $B(m,n)$ is the beta function. The values of the parameters depend on shower size (N_e), depth in the atmosphere, identity of the primary nucleus, etc. For showers with $N_e \approx 10^6$ at sea level, Greisen uses $s = 1.25$, $d = 1$, and $C_2 = 0.088$. For showers with average $N_e \approx 6\times10^7$ at the Akeno array [109], $d = 1.3$, $C_2 = 0.2$ and s is fitted for each shower with typical values between 0.95 and 1.15. Finally, x is r/r_1, where r_1 is the Molière radius, which depends on the density of the atmosphere and hence on the altitude at which showers are detected. At sea level $r_1 \approx 78$ m, and it increases with altitude as the air density decreases. (See the section on electromagnetic cascades in the article on the passage of particles through matter in this *Review*).

The lateral spread of a shower is determined largely by Coulomb scattering of the many low-energy electrons and is characterized by the Molière radius, which depends on density and thus on temperature and pressure. The lateral spread of the muons (ρ_μ) is larger and depends on the transverse momenta of the muons at production as well as multiple scattering.

There are large fluctuations in development from shower to shower, even for showers initiated by primaries of the same energy and mass—especially for small showers, which are usually well

past maximum development when observed at the ground. Thus the shower size N_e and primary energy E_0 are only related in an average sense, and even this relation depends on depth in the atmosphere. One estimate of the relation is [109]

$$E_0 \sim 3.9 \times 10^6 \mathrm{GeV} (N_e/10^6)^{0.9} \tag{30.12}$$

for vertical showers with $10^{14} < E < 10^{17}$ eV at 920 g cm^{-2} (965 m above sea level). As E_0 increases, the shower maximum (on average) moves down into the atmosphere and the relation between N_e and E_0 changes. Moreover, because of fluctuations, N_e as a function of E_0 is not correctly obtained by inverting Eq. (30.12). At the maximum of shower development, there are approximately 0.66 particles per GeV of primary energy.

The muon and electron lateral distributions used in reconstructing experimental data must be adapted taking into consideration the altitude of the observations and the characteristics of the detectors used. Useful examples include the Akeno [109] and Volcano Ranch [121] arrays. Compilations of useful lateral distribution functions and discussion of their applications are given in Refs. [122, 123].

Cosmic ray shower development is sensitive to hadronic physics in the forward region above energies that can be probed at accelerators. Specialized simulation codes such as CORSIKA [124] include both the relevant physics and methods for efficiently dealing with the large number of particles in high energy air showers. Hadronic interaction models used to interpret air shower measurements now incorporate data from the LHC, reducing the extrapolation required. However, differences between the simulated and observed properties of showers remain. Most notably, the observed muon content of showers near 10^{19} eV exceeds that given by models by 30–60% [125].

There are three common types of air shower detectors: shower arrays that measure a ground parameter related to shower size N_e and muon number N_μ as well as the lateral distribution on the ground, optical Cherenkov and radio detectors that detect forward-beamed emission by the charged particles of the shower, and 'fluorescence' detectors that measure nitrogen scintillation excited by the charged particles in the shower. The fluorescence light is emitted isotropically so the showers can be observed from the side. Detection of radiofrequency emission from showers via geomagnetic and Askaryan mechanisms has been successfully employed in recent experiments [126]. Detailed simulations and cross-calibrations between different types of detectors are necessary to establish the primary energy spectrum from air-shower experiments.

Figure 30.9 shows the "all-particle" spectrum. The differential energy spectrum has been multiplied by $E^{2.6}$ in order to display the features of the steep spectrum that are otherwise difficult to discern. The steepening that occurs between 10^{15} and 10^{16} eV is known as the *knee* of the spectrum. Another steepening occurs around 10^{17} eV, known as the *second knee*. The feature around $10^{18.5}$ eV is called the *ankle* of the spectrum.

Cosmic ray experiments have systematic differences in their energy scales. For ground-based air-shower arrays, these are dependent on an assumed composition and on the hadronic interaction model used when interpreting the data. Systematic errors in energy scale are simplest when plotting $\frac{dN}{d\ln E} = E\frac{dN}{dE}$. When the spectrum is multiplied by a different power of energy, systematic errors in energy scale result in an apparent shift in the normalization of the spectrum; for example, when the spectrum is multiplied by $E^{2.6}$ a systematic shift of 10% in the energy scale results in a 16% change in the normalization of the plotted flux. See Ref. [64],§2.5.2 for further discussion of this issue.

In the energy range above 10^{17} eV, the fluorescence technique [127] is particularly useful because it can establish the primary energy in a nearly model-independent way by observing most of the longitudinal development of each shower, from which E_0 is obtained by integrating the energy

deposition in the atmosphere. The result, however, depends strongly on the light absorption in the atmosphere and the calculation of the aperture of the detector.

Assuming the cosmic-ray spectrum below 10^{18} eV is of Galactic origin, the knee could indicate that most cosmic accelerators in the Galaxy have reached their maximum energy for acceleration of protons. Some types of expanding supernova remnants, for example, are estimated not to be able to accelerate protons above energies in the range of 10^{15} eV. Further observations of the PeV gamma-ray sources recently detected by LHAASO [128] may provide insight into the types of objects that act as Galactic sources near the knee and energies to which they can accelerate cosmic rays. Effects of propagation and confinement in the Galaxy [129] also need to be considered. A discussion of models of the knee may be found in Ref. [130].

The second knee may have a similar origin to the knee, but corresponding to steepening of the spectrum of heavy nuclei, particularly iron. The Kascade-Grande experiment has reported observation of a second steepening of the spectrum near 8×10^{16} eV, with evidence that this structure is accompanied by a transition to electron-poor showers resulting from heavy primaries [112]. Kascade Grande has also reported that the spectrum of light nuclei is steeper than the all-particle spectrum below the second knee and flattens in the vicinity of the second knee [131]. IceCube has performed a composition analysis using coincident surface (IceTop) and in-ice data, and finds that the mean logarithmic mass increases between 5×10^{15} eV and 10^{17} eV [132]. Together, these data are suggestive that the knee and second knee may result from a *Peters cycle*, with a steepening of the spectrum of each primary element taking place at the same rigidity but different energy per particle [133].

The Auger Observatory and Telescope Array (TA) have studied composition using the depth of shower maximum X_{max}, a quantity that correlates strongly with $\ln E/A$ and with the interaction cross section of the primary particle. The Auger Collaboration [134], using a post-LHC hadronic interaction model, reports a light composition below 2×10^{18} eV and becoming heavier above that energy, with the mean mass intermediate between protons and iron at 3×10^{19} eV. The TA Collaboration [135], using a different post-LHC model, has interpreted their data as implying a light primary composition (mainly p and He) of ultrahigh-energy cosmic-rays (UHECR) from 1.3×10^{18} to 4×10^{19} eV. The Auger and TA Collaborations have also conducted a thorough joint analysis [136] and state that, at the current level of statistics and understanding of systematics, both data sets are compatible with being drawn from the same parent distribution, and that the TA data is compatible both with a light composition below 10^{19} eV and with the mixed composition above 10^{19} eV as reported by the Auger Collaboration.

Possible contributions to the origin of the ankle include a higher energy population of particles overtaking a lower energy population, for example an extragalactic flux beginning to dominate over the Galactic flux (e.g. Ref. [127]). Another proposed mechanism is that the dip structure in the region of the ankle is due to $p\gamma \rightarrow e^+ + e^-$ energy losses of extragalactic protons on the 2.7 K cosmic microwave radiation (CMB) [137]. The latter mechanism requires that the composition in this energy range is predominantly protons. A study of the correlation between the depth of shower maximum and the surface detector singal in hybrid showers by the Auger Collaboration favors a mixed composition at the ankle, disfavoring the dip model [138].

The propagation of the highest energy cosmic rays over extragalactic distances is predicted to result in a rapid steepening of the spectrum (called the GZK feature) around 5×10^{19} eV, resulting from the onset of inelastic interactions of UHE cosmic rays with the cosmic microwave background [140, 141]. Photo-dissociation of heavy nuclei in the mixed composition model [142] would have a similar effect. The HiRes detector, Auger Observatory, and the Telescope Array have all detected evidence of a suppression consistent with the GZK effect [114–116, 118, 143], with a steepened spectrum extending beyond 10^{20} eV. The differential energy spectra measured by the

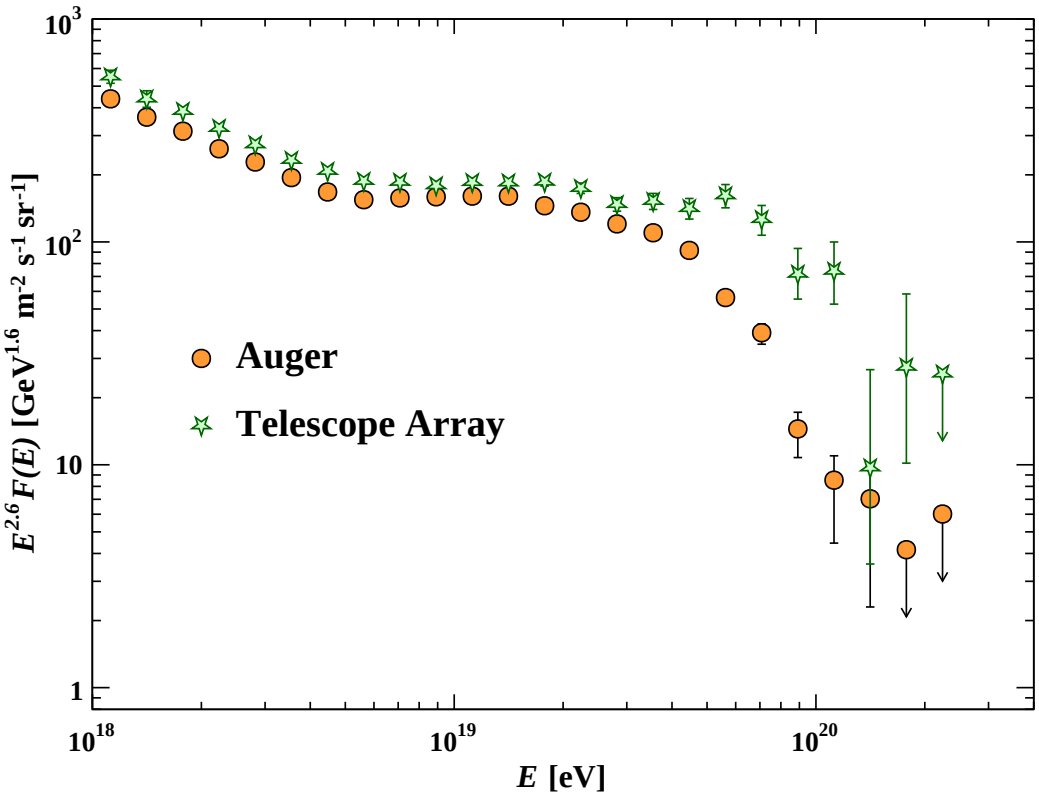

Figure 30.10: Expanded view of the highest energy portion of the cosmic-ray spectrum from data of the Pierre Auger Observatory [115–117, 139] and the Telescope Array [118, 119]. The small difference in the normalization of the spectra corresponds to a difference in energy scale of 9%.

TA and Auger collaborations agree within systematic errors except at the very highest energies (Fig. 30.10). Both collaborations have also reported evidence for a steepening of the spectrum around $10^{19.2}$ eV, dubbed the 'instep' [115, 144].

Cosmic rays above 5×10^{19} eV are predominantly from nearby sources (<100 Mpc). Differences between the Auger Observatory and Telescope Array spectra above this energy may reflect differences in the spectra between the northern and southern hemispheres. The Auger Collaboration has reported the observation of a dipole of amplitude $6.6^{+1.2}_{-0.8}\%$ for cosmic rays with energies above 8×10^{18} eV. The direction of the dipole indicates an extragalactic origin for these particles [145–147]. There are also hints of structure at smaller angular scales. TA has reported a 'hot spot' in the Northern Hemisphere at energies above 5.7×10^{19} eV of radius $\sim20^\circ$ with a chance probability of this excess with respect to an isotropic distribution of 3.7×10^{-4} [148]. The Auger Collaboration has also reported an excess of events above 3.7×10^{19} eV in a region near the radio-loud active galaxy Centaurus A with a post-trial significance of 3.9σ, and a correlation of the distribution of ultrahigh energy events with several catalogs of nearby astrophysical objects, with starburst galaxies giving the highest significance at 4.5σ [149]. TA has also observed a similar correlation of cosmic arrival directions above 4.9×10^{19} eV with starburst galixies with a significance of 4.3σ [148].

30.6 Gamma Rays

There is a well-studied flux of cosmic gamma rays (gamma rays defined here as having energy greater than 1 MeV) present at the top of the atmosphere. This flux has been measured with

multiple space and ground-based instruments [Cite PDG 36.2.2] across a broad range of energies.

Contributions to the flux include steady and transient emissions from numerous Galactic and extragalactic sources, as well as diffuse components originating from both inside and outside the Galaxy. The source-associated contributions include photons from a range of objects and phenomena such as supernova remnants, pulsars, active galactic nuclei, GRBs, and more. These contributions have been well documented in reviews (e.g., [150]) and in catalogs in the MeV [151, 152] GeV [153] and TeV [154] energy ranges. LHAASO has recently observed photon spectra from several sources extending to ~ 1 PeV and beyond [128, 155].

The majority of photons detected at higher energies are characterized as diffuse emission unassociated with discrete sources. The Large Area Telescope (LAT) of the Fermi Gamma-Ray Space Telescope has examined this radiation in detail for energies above 50 MeV [156]. The dominant component comes from the plane of the Galaxy (i.e., $|b| \lesssim 10$ deg) and is referred to as the Galactic diffuse emission. It can be attributed largely to interactions of high energy cosmic hadrons and electrons with interstellar matter and photon fields, leading to emission from π^0 decay, inverse Compton scattering and bremsstrahlung [153, 157]. Ground-based all-sky gamma detectors have extended these measurements to TeV energies and beyond in certain regions of the Galactic Plane [158–160].

In addition to the Galactic flux, there is a lower-intensity component to the diffuse emission that appears to be isotropic across the sky. This is thought to be extragalactic in origin and is often referred to as the isotropic gamma-ray background (IGRB). The IGRB has been measured by the LAT above 100 MeV and has an energy spectrum that can be described by a power-law with index -2.3 and an exponential cutoff at approximately 280 GeV, with a total intensity of $(7.2 \pm 0.6) \times 10^{-6} \mathrm{cm}^{-2}\mathrm{s}^{-1}\mathrm{sr}^{-1}$ [161]. Above energies of tens of TeV most emission is likely of local origin, due to Mpc and shorter attenuation lengths for interactions with cosmic microwave and infrared photons fields - this is referred to as the gamma-ray horizon [162, 163].

30.7 High-Energy Astrophysical Neutrinos

Neutrinos are expected to be produced in hadronic interactions in a variety of astrophysical objects. IceCube has reported a population of astrophysical neutrino events extending from tens of TeV to beyond ten PeV [164, 173, 174]. Multimessenger observations of the flaring blazar TXS 0506+056 have identified this object as a high-energy neutrino source [175, 176].

There is also expected to be a neutrino flux produced in cosmic ray GZK interactions. Measuring this *cosmogenic*[4] neutrino flux above 10^{18} eV would help resolve the UHECR uncertainties mentioned above. One half of the energy that UHECR protons lose in photoproduction interactions that cause the GZK effects ends up in neutrinos [177]. Heavier nuclei produce lower energy neutrinos due to the lower energy of their constituent nucleons. The magnitude of the cosmogenic neutrino flux depends strongly on the cosmic-ray spectrum at acceleration, the cosmic-ray composition, the cosmological evolution of the cosmic-ray sources, and the energy of the Galactic-extragalactic transition.

The expected rate of cosmogenic neutrinos is lower than current limits obtained by IceCube [164],the Auger Observatory [167], RICE [166,178], and ANITA [168], which are shown in Fig. 30.11 together with a models for cosmogenic neutrino production [171, 172] and the Waxman-Bahcall benchmark flux of neutrinos produced in cosmic ray sources [169,170]. At production, the dominant component of neutrinos comes from $\pi^{\pm}$ decays and has flavor content ν_e:ν_μ:ν_τ = 1:2:0. After oscillations, the arriving cosmogenic neutrinos are expected to be a 1:1:1 mixture of flavors. The sensitivity of each experiment depends on neutrino flavor, and all limits are expressed as three-flavor limits assuming a 1:1:1 mixture.

[4]Here we use cosmogenic to denote neutrinos produced by photoproduction during propagation, and astrophysical to denote neutrinos produced by other mechanisms or close to sources.

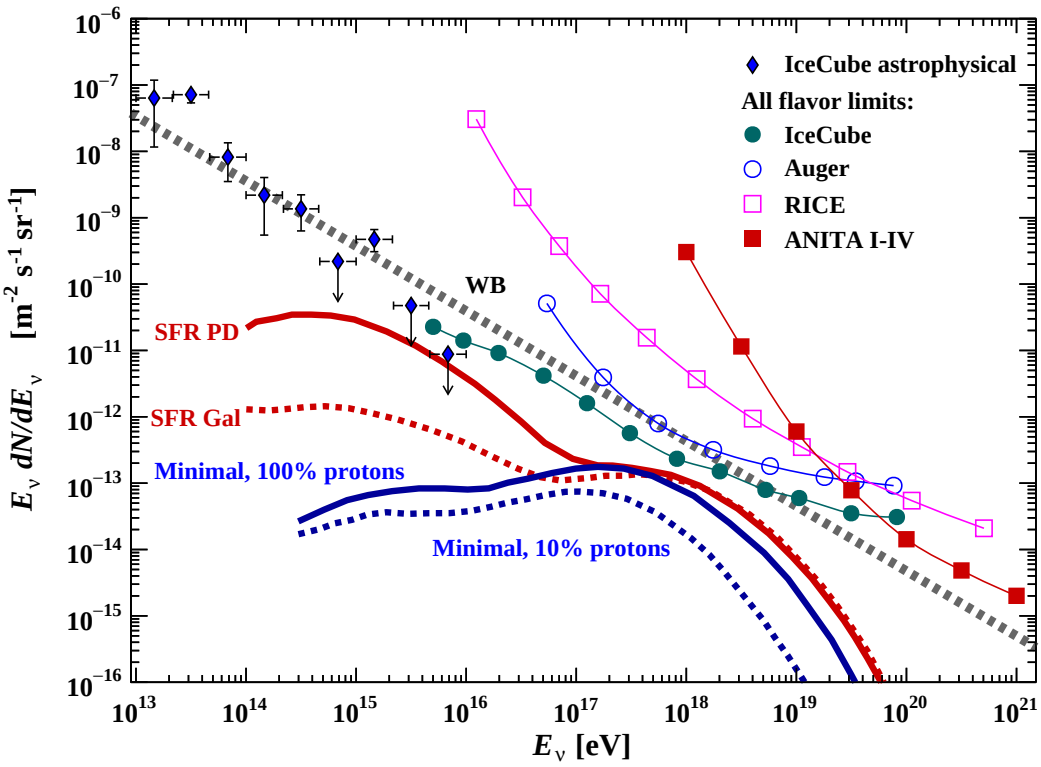

Figure 30.11: The best-fit IceCube *astrophysical* all-flavor neutrino flux [164]. Also shown are differential limits on the flux of *cosmogenic* neutrinos set by four experiments [165–168] The IceCube limit on cosmogenic neutrinos accounts for a nuisance background of astrophysical neutrinos. The curves show the Waxman-Bahcall benchmark flux (solid grey) [169, 170], cosmogenic models with cosmic ray sources with maximum proton energy of $10^{20.5}$ eV evolving with the star-formation rate in proton dip (solid red) and Galactic composition (dashed red) scenarios [171], and 'minimal' cosmogenic models with protons constituting 100% (solid blue) and 10% (dashed red) of the cosmic rays [172].

References

[1] O. Adriani *et al.* (PAMELA), Science **332**, 69 (2011).
[2] M. Aguilar *et al.* (AMS), Phys. Rev. Lett. **114**, 171103 (2015).
[3] M. Aguilar *et al.* (AMS), Phys. Rev. Lett. **115**, 21, 211101 (2015).
[4] K. Abe *et al.*, Astrophys. J. **822**, 2, 65 (2016).
[5] M. J. Christ *et al.*, Astrophys. J. **502**, 278 (1998).
[6] A.D. Panov *et al.* (ATIC Collab.), Bull. Russian Acad. of Science, Physics, **73**, 564 (2009).
[7] V. A. Derbina *et al.* (RUNJOB), Astrophys. J. **628**, L41 (2005).
[8] H. S. Ahn *et al.*, Astrophys. J. **707**, 593 (2009).
[9] J.J. Engelmann *et al.* (HEAO3-C2 Collab.), Astron. & Astrophys. **233**, 96 (1990).
[10] D. Müller *et al.* (CRN Collab.), Astrophys. J. **374**, 356 (1991).
[11] M. Ave *et al.*, Astrophys. J. **678**, 262 (2008).
[12] F. Aharonian *et al.* (H.E.S.S.), Phys. Rev. **D75**, 042004 (2007).
[13] A. Archer *et al.* (VERITAS), Phys. Rev. **D98**, 2, 022009 (2018).

[14] M. Aguilar *et al.*, Phys. Rev. Lett. **124**, 21, 211102 (2020).
[15] M. Aguilar *et al.*, Phys. Rev. Lett. **126**, 4, 041104 (2021).
[16] D. Maurin *et al.*, Astron. & Astrophys. **569**, A32 (2014).
[17] M. Aguilar *et al.* (AMS), Phys. Rev. Lett. **119**, 25, 251101 (2017).
[18] K. Lave *et al.*, Astrophys. J. **770**, 117 (2013).
[19] G. DeNolfo *et al.*, Adv. Space Res. **38**, 1558 (2006).
[20] R. Murphy *et al.*, Astrophys. J. **831**, 148 (2016).
[21] B. Rauch *et al.*, Astrophys. J. **697**, 2083 (2009).
[22] K. Lodders, H. Palme and H.P.Gail, *Landolt-Börnstein, New Series*, volume VI/4b, chapter 4.4, 560, Springer-Verlag (2009).
[23] A. W. Strong, I. V. Moskalenko and V. S. Ptuskin, Ann. Rev. Nucl. Part. Sci. **57**, 285 (2007).
[24] R.A. Mewaldt *et al.*, Space Science Reviews 99,27(2001).
[25] O. Adriani *et al.* (PAMELA), Phys. Rev. Lett. **106**, 201101 (2011).
[26] M. Boezio *et al.*, Astrophys. J. **532**, 653 (2000).
[27] M. Aguilar *et al.* (AMS), Phys. Rev. Lett. **122**, 10, 101101 (2019).
[28] S. Abdollahi *et al.* (Fermi-LAT), Phys. Rev. **D95**, 8, 082007 (2017).
[29] G. Ambrosi *et al.* (DAMPE), Nature **552**, 63 (2017).
[30] O. Adriani *et al.* (CALET), Phys. Rev. Lett. **122**, 18, 181102 (2019).
[31] F. Aharonian *et al.* (H.E.S.S.), Phys. Rev. Lett. **101**, 261104 (2008).
[32] F. Aharonian *et al.* (H.E.S.S.), Astron. Astrophys. **508**, 561 (2009).
[33] A. Archer *et al.* (VERITAS), Phys. Rev. **D98**, 6, 062004 (2018).
[34] Y. Shikaze *et al.*, Astropart. Phys. **28**, 154 (2007).
[35] A. A. Abdo *et al.*, Astrophys. J. **698**, 2121 (2009).
[36] A. U. Abeysekara *et al.* (HAWC, IceCube), Astrophys. J. **871**, 1, 96 (2019).
[37] M. Amenomori *et al.*, Astrophys. J. **711**, 119 (2010).
[38] M. G. Aartsen *et al.*, Astrophys. J. **826**, 2, 220 (2016), [arXiv:1603.01227].
[39] M. Amenomori *et al.*, Astrophys. J. **836**, 2, 153 (2017), [arXiv:1701.07144].
[40] M. Ahlers and P. Mertsch, Progr. Part. and Nucl. Phys. **94**, 184 (2017), [arXiv:1612.01873].
[41] O. Adriani *et al.* (PAMELA), Nature **458**, 607 (2009).
[42] O. Adriani *et al.*, Phys. Rev. Lett. **102**, 051101 (2009).
[43] J.J. Beatty *et al.*, Phys. Rev. Lett. **93**, 24112 (2004).
[44] I. V. Moskalenko and A. W. Strong, Astrophys. J. **493**, 694 (1998).
[45] A. Ibarra, D. Tran and C. Weniger, Int. J. Mod. Phys. **A28**, 1330040 (2013).
[46] D. Gaggero *et al.*, Phys. Rev. Lett. **111**, 021102 (2013).
[47] P.-F. Yin *et al.*, Phys. Rev. **D88**, 2, 023001 (2013).
[48] M. Aguilar *et al.* (AMS), Phys. Rev. Lett. **110**, 141102 (2013).
[49] L. Accardo *et al.* (AMS), Phys. Rev. Lett. **113**, 121101 (2014).
[50] J. Nishimura *et al.*, Adv. Space Research **19**, 767 (1997).
[51] A. S. Beach *et al.*, Phys. Rev. Lett. **87**, 271101 (2001).

[52] A. Yamamoto *et al.*, Adv. Space Research**42**, 443(2008).

[53] Y. Asaoka *et al.*, Phys. Rev. Lett. **88**, 51101 (2002).

[54] K. Abe *et al.*, Phys. Rev. Lett. **108**, 131301 (2012).

[55] H. Fuke *et al.*, Phys. Rev. Lett. **95**, 081101 (2005).

[56] I. Cholis, D. Hooper and T. Linden, Phys. Rev. **D93**, 4, 043016 (2016).

[57] R. Bellotti *et al.*, Phys. Rev. **D53**, 35 (1996).

[58] R. Bellotti *et al.* (WiZard/MASS2), Phys. Rev. **D60**, 052002 (1999).

[59] M. Boezio *et al.* (WiZard/CAPRICE), Phys. Rev. **D62**, 032007 (2000).

[60] M. Boezio *et al.*, Phys. Rev. **D67**, 072003 (2003).

[61] S. Coutu *et al.*, Phys. Rev. **D62**, 032001 (2000).

[62] S. Haino *et al.*, Phys. Lett. **B594**, 35 (2004).

[63] T. Sanuki *et al.*, Phys. Rev. **D75**, 043005 (2007).

[64] T.K. Gaisser, R. Engel, and E. Resconi, *Cosmic Rays and Particle Physics (second edition)*, Cambridge University Press (2016).

[65] P. Lipari, Astropart. Phys. **1**, 195 (1993).

[66] E. Mocchiutti *et al.*, in *Proc. 28th Int. Cosmic Ray Conf.*, Tsukuba, 1627 (2003). [http://adsabs.harvard.edu/abs/2003ICRC....3.1627M].

[67] M. P. De Pascale *et al.*, J. Geophys. Res. **98**, A3, 3501 (1993).

[68] P.K.F. Grieder, *Cosmic Rays at Earth*, Elsevier Science (2001).

[69] J. Kremer *et al.*, Phys. Rev. Lett. **83**, 4241 (1999).

[70] P. Achard *et al.* (L3), Phys. Lett. **B598**, 15 (2004).

[71] O. C. Allkofer, K. Carstensen and D. W. Dau, Phys. Lett. **36B**, 425 (1971).

[72] B. C. Rastin, J. Phys. **G10**, 1609 (1984).

[73] C. A. Ayre *et al.*, J. Phys. **G1**, 584 (1975).

[74] H. Jokisch *et al.*, Phys. Rev. **D19**, 1368 (1979).

[75] C. G. S. Costa, Astropart. Phys. **16**, 193 (2001).

[76] P. Adamson *et al.* (MINOS), Phys. Rev. **D76**, 052003 (2007).

[77] S. Hayakawa, *Cosmic Ray Physics*, Wiley, Interscience, New York (1969).

[78] R.R. Daniel and S.A. Stephens, Revs. Geophysics & Space Sci. **12**, 233 (1974).

[79] K.P. Beuermann and G. Wibberenz, Can. J. Phys. **46**, S1034 (1968).

[80] I. S. Diggory *et al.*, J. Phys. **A7**, 741 (1974).

[81] V. Khachatryan *et al.* (CMS), Phys. Lett. **B692**, 83 (2010).

[82] N. Agafonova *et al.* (OPERA), Eur. Phys. J. **C67**, 25 (2010).

[83] P. Lipari and T. Stanev, Phys. Rev. **D44**, 3543 (1991).

[84] M. Crouch, in *Proc. 20th Int. Cosmic Ray Conf.*, Moscow, **6**, 165 (1987) [http://adsabs.harvard.edu/abs/1987ICRC....6..165C].

[85] Yu.M. Andreev, V.I. Gurentzov, and I.M. Kogai, in *Proc. 20th Int. Cosmic Ray Conf.*, Moscow, **6**, 200 (1987), [http://adsabs.harvard.edu/abs/1987ICRC....6..200A].

[86] M. Aglietta *et al.* (LVD), Astropart. Phys. **3**, 311 (1995).

[87] M. Ambrosio *et al.* (MACRO), Phys. Rev. **D52**, 3793 (1995).

[88] C. Berger *et al.* (FREJUS), Phys. Rev. **D40**, 2163 (1989).

[89] C. Waltham *et al.*, in *Proc. 27th Int. Cosmic Ray Conf.*, Hamburg, 991 (2001), [http://adsabs.harvard.edu/abs/2001ICRC....3..991W].

[90] I. A. Belolaptikov *et al.* (BAIKAL), Astropart. Phys. **7**, 263 (1997).

[91] J. Babson *et al.* (DUMAND), Phys. Rev. **D42**, 3613 (1990).

[92] P. Desiati *et al.*, in *Proc. 28th Int. Cosmic Ray Conf.*, Tsukuba, 1373 (2003) [http://adsabs.harvard.edu/abs/2003ICRC....3.1373D].

[93] T. Pradier (ANTARES), in "Proceedings, 43rd Rencontres de Moriond on Electroweak Interactions and Unified Theories: La Thuile, Italy, March 1-8, 2008," 423–430 (2008).

[94] S. Aiello *et al.* (NEMO), Astropart. Phys. **66**, 1 (2015).

[95] F. Reines *et al.*, Phys. Rev. Lett. **15**, 429 (1965).

[96] M.M. Boliev *et al.*, in *Proc. 3rd Int. Workshop on Neutrino Telescopes* (ed. Milla Baldo Ceolin), 235 (1991).

[97] M. Ambrosio *et al.* (MACRO), Phys. Lett. **B434**, 451 (1998).

[98] F. Ronga (MACRO), in "Proceedings, 26th International Cosmic Ray Conference (ICRC), August 17-25, 1999, Salt Lake City: Invited, Rapporteur, and Highlight Papers," volume 2, 172 (1999), URL http://krusty.physics.utah.edu/~icrc1999/root/vol2/h4_1_07.pdf.

[99] R. Becker-Szendy *et al.*, Phys. Rev. Lett. **69**, 1010 (1992).

[100] *Proc. 25th Int. Conf. High-Energy Physics*, Singapore (eds. K.K. Phua and Y. Yamaguchi, World Scientific), 662 1991.

[101] S. Hatakeyama *et al.* (Kamiokande), Phys. Rev. Lett. **81**, 2016 (1998).

[102] Y. Fukuda *et al.* (Super-Kamiokande), Phys. Rev. Lett. **82**, 2644 (1999).

[103] Y. Fukuda *et al.* (Super-Kamiokande), Phys. Rev. Lett. **81**, 1562 (1998).

[104] T. Futagami *et al.* (Super-Kamiokande), Phys. Rev. Lett. **82**, 5194 (1999).

[105] Y. Ashie *et al.* (Super-Kamiokande), Phys. Rev. **D71**, 112005 (2005).

[106] R. Alfaro *et al.* (HAWC), Phys. Rev. **D96**, 12, 122001 (2017).

[107] Yu. A. Fomin *et al.*, *Proc. 22nd Int. Cosmic Ray Conf.*, Dublin, **2**, 85 (1991) [http://adsabs.harvard.edu/abs/1991ICRC....2...85F].

[108] M. Amenomori *et al.*, Astrophys. J. **268**, 1165 (2008).

[109] M. Nagano *et al.*, J. Phys. **G10**, 1295 (1984).

[110] M. A. K. Glasmacher *et al.*, Astropart. Phys. **10**, 291 (1999).

[111] T. Antoni *et al.* (KASCADE), Astropart. Phys. **24**, 1 (2005).

[112] W. D. Apel *et al.* (KASCADE Grande), Phys. Rev. Lett. **107**, 171104 (2011).

[113] K. Andeen, M. Plum *et al.*, (IceCube Collab.), *Proceedings of Science* (ICRC2019), 172 (2019).

[114] R. U. Abbasi *et al.* (HiRes), Phys. Rev. Lett. **100**, 101101 (2008).

[115] A. Aab *et al.* (Pierre Auger), Phys. Rev. Lett. **125**, 12, 121106 (2020), [arXiv:2008.06488].

[116] A. Aab *et al.* (Pierre Auger), Phys. Rev. D **102**, 6, 062005 (2020), [arXiv:2008.06486].

[117] P. Abreu *et al.*, Eur. Phys, J. C **81** (2021).

[118] D. Ivanov *et al.*, (Telescope Array Collab.), *Proceedings of Science* (ICRC2019), 298 (2019).

[119] R. U. Abbasi *et al.* (Telescope Array), Astrophys. J. **865**, 1, 74 (2018), [arXiv:1803.01288].

[120] K. Greisen, Ann. Rev. Nucl. Sci. **10**, 63 (1960).

[121] J. Linsley, *Proc. 15th. Internat. Cosmic Ray Conf. (Plovdiv)*, **12**, 56-65, 89-96. (Available from ADS).

[122] M. Nagano and A. Watson, Rev. Mod. Phys. **72**, 689 (2000).

[123] A. Haungs *et al.*, Rep. Prog. Phys. (2003).

[124] Https://www.iap.kit.edu/corsika/.

[125] A. Aab *et al.* (Pierre Auger), Phys. Rev. Lett. **117**, 19, 192001 (2016).

[126] T. Huege, Phys. Rept. **620**, 1 (2016).

[127] D. J. Bird *et al.* (HiRes), Astrophys. J. **424**, 491 (1994).

[128] Z. Cao *et al.*, Nature **594**, 7861, 33 (2021).

[129] V.S. Ptuskin *et al.*, Astron. & Astrophys. **268**, 726 (1993).

[130] J. R. Hoerandel, Astropart. Phys. **21**, 241 (2004).

[131] W. D. Apel *et al.*, Phys. Rev. **D87**, 081101 (2013), [arXiv:1304.7114].

[132] M. G. Aartsen *et al.* (IceCube) (2019), [arXiv:1906.04317].

[133] B. Peters, Nuovo Cimento **XXII**, 800 (1961).

[134] J. Bellido *et al.* (Auger Collab.), Proceedings of Science(ICRC2017), 506 (2017).

[135] D. Ikeda *et al.* (TA Collab.), Proceedings of Science(ICRC2017), 515 (2017).

[136] V. de Souza *et al.* (TA and Auger Collabs.), Proceedings of Science(ICRC2017), 522 (2017).

[137] V. Berezinsky, A. Z. Gazizov and S. I. Grigorieva, Phys. Rev. **D74**, 043005 (2006).

[138] A. Aab *et al.* (Pierre Auger), Phys. Lett. B **762**, 288 (2016), [arXiv:1609.08567].

[139] V. Novotny *et al.*, (Auger Collab.), *Proceedings of Science* (ICRC2021), 324 (2021).

[140] K. Greisen, Phys. Rev. Lett. **16**, 748 (1966).

[141] G. T. Zatsepin and V. A. Kuzmin, JETP Lett. **4**, 78 (1966), [Pisma Zh. Eksp. Teor. Fiz.4,114(1966)].

[142] D. Allard *et al.*, Astron. & Astrophys. **443**, L29 (2005).

[143] R. U. Abbasi *et al.* (HiRes), Astropart. Phys. **32**, 53 (2009).

[144] D. Ivanov *et al.*, *Proceedings of Science* (ICRC2021), 341(2021).

[145] A. Aab *et al.*, Science **357**, 1266 (2017).

[146] A. Aab *et al.*, Astrophys. J. **868**, 1 (2018).

[147] E. Roulet *et al.*, (Auger Collab.), *Proceedings of Science* (ICRC2019), 408 (2019.

[148] T. Fujii*et al.*, (Telescope Array Collab.), *Proceedings of Science* (ICRC2021), 392 (2021).

[149] L. Caccianiga *et al.*, (Auger Collab.), *Proceedings of Science* (ICRC2019), 206 (2019).

[150] A. De Angelis and M. Mallamaci, European Physical Journal Plus **133**, 8, 324 (2018), [arXiv:1805.05642].

[151] V. Schönfelder *et al.*, Astron. Astrophys. Suppl. **143**, 145 (2000), [arXiv:astro-ph/0002366].

[152] I. S. D. Centre, "Integral general reference catalog," `https://www.isdc.unige.ch/integral/science/catalogue`.

[153] S. Abdollahi *et al.*, Astrophys. J. Suppl. **247**, 1, 33 (2020), [arXiv:1902.10045].

[154] S. Wakely and D. Horan, "Tevcat," `http://tevcat.uchicago.edu`.

[155] Z. Cao *et al.*, Science **373**, 6553, 425 (2021).

[156] M. Ackermann *et al.*, Astrophys. J. **750**, 1, 3 (2012), [arXiv:1202.4039].

[157] F. Acero *et al.*, Astrophys. J. Suppl. **223**, 2, 26 (2016), [arXiv:1602.07246].

[158] R. Atkins *et al.*, Phys. Rev. Lett. **95**, 25, 251103 (2005), [arXiv:astro-ph/0502303].

[159] B. Bartoli *et al.*, Astrophys. J. **806**, 1, 20 (2015), [arXiv:1507.06758].

[160] M. Amenomori *et al.*, Phys. Rev. Lett. **126**, 14, 141101 (2021), [arXiv:2104.05181].

[161] M. Ackermann *et al.*, Astrophys. J. **799**, 1, 86 (2015), [arXiv:1410.3696].

[162] T. M. Kneiske, K. Mannheim and D. H. Hartmann, in S. Ritz, N. Gehrels and C. R. Shrader, editors, "Gamma 2001: Gamma-Ray Astrophysics," volume 587 of *American Institute of Physics Conference Series*, 358–362 (2001).

[163] S. P. Wakely, in S. R. Magill and R. Yoshida, editors, "Calorimetry in High Energy Physics: XII," volume 867 of *American Institute of Physics Conference Series*, 139–147 (2006).

[164] M. G. Aartsen *et al.* (IceCube), Astrophys. J. **809**, 1, 98 (2015).

[165] M. G. Aartsen *et al.* (IceCube), Phys. Rev. **D98**, 6, 062003 (2018).

[166] I. Kravchenko *et al.*, Phys. Rev. **D85**, 062004 (2012).

[167] F. Pedriera *et al.*, (Auger Collab.), *Proceedings of Science* (ICRC2019), 172 (2019).

[168] C. Deaconu *et al.*, (ANITA Collab.), *Proceedings of Science* (ICRC2019), 867 (2019).

[169] E. Waxman and J. N. Bahcall, Phys. Rev. **D59**, 023002 (1999).

[170] E. Waxman, *The Origin of IceCube's Neutrinos: Cosmic Ray Accelerators Embedded in Star Forming Calorimeters* (2017), [arXiv:1511.00815].

[171] K. Kotera, D. Allard and A. V. Olinto, JCAP **1010**, 013 (2010).

[172] M. Ahlers and F. Halzen, Phys. Rev. **D86**, 083010 (2012).

[173] M. G. Aartsen *et al.* (IceCube), Science **342**, 1242856 (2013).

[174] M. G. Aartsen *et al.* (IceCube), Phys. Rev. Lett. **113**, 101101 (2014).

[175] M. G. Aartsen *et al.* (IceCube, Fermi-LAT, MAGIC, AGILE, ASAS-SN, HAWC, H.E.S.S., INTEGRAL, Kanata, Kiso, Kapteyn, Liverpool Telescope, Subaru, Swift NuSTAR, VERITAS, VLA/17B-403), Science **361**, eaat1378 (2018).

[176] M. G. Aartsen *et al.* (IceCube), Science **361**, 6398, 147 (2018).

[177] V. S. Berezinsky and G. T. Zatsepin, Phys. Lett. **28B**, 423 (1969).

[178] I. Kravchenko *et al.*, Phys. Rev. **D73**, 082002 (2006).